Acta Cryst C STRUCTURAL CHEMISTRY

ISSN 2053-2296

Bonding properties and crystal packing in β-$(SeCl_4)_4$ derived from Hirshfeld Atom Refinement

Juan de Dios Guzmán-Hernández[a,b] and Vojtech Jancik[a,b]*

[a]Universidad Nacional Autónoma de México, Instituto de Química, Ciudad Universitaria, Ciudad de México, 04510, Mexico, and [b]Centro Conjunto de Investigación en Química Sustentable UAEM–UNAM, Carr. Toluca-Atlacomulco km 14.5, 50200 Toluca, Estado de México, Mexico. *Correspondence e-mail: vjancik@iquimica.unam.mx

Received 29 July 2024
Accepted 28 October 2024

Edited by M. Rosales-Hoz, Cinvestav, Mexico

This article is part of the collection *Crystallography in Latin America: a vibrant community*.

Keywords: selenium chloride; crystal structure; HAR; Hirshfeld; deformation density; QTAIM; IAM; chalcogen chemistry; heterocubane core.

CCDC reference: 2394345

Supporting information: this article has supporting information at journals.iucr.org/c

Binary chalcogen halogen EX_4 species represent intriguing systems in terms of chemical bonding theories, such as hypervalency and stereoactivity of lone electron pairs. Instead of a simple molecular EX_4 structure, selenium tetrachloride forms an ionic pair, $Cl_3Se^+Cl^-$, that assembles into a tetrameric $(SeCl_4)_4$ structure, namely, tetra-μ_3-chlorido-dodecachloridotetraselenium. This article describes the charge–density analysis of the tetrameric molecule of β-$SeCl_4$ based on the aspherical model obtained from Hirshfeld Atom Refinement of the tetrameric molecule and of an explicit cluster of 15 tetramers that simulates the crystal packing. Deformation density, electron localization function (ELF) and Quantum Theory of Atoms in Molecules (QTAIM) were used to evaluate the bonding situation, the electron-density distribution around the Se atom and the interaction energy of the tetramer.

1. Introduction

Binary chalcogen halogen compounds are the cornerstone of chalcogen chemistry as they are easily obtainable and serve as primary reagents for further synthesis. Furthermore, they feature a rich structural chemistry, where the EX_4 (E = chalcogen and X = halogen) species attracted much attention (Greenwood & Earnshaw, 1997). According to VSEPR (valence shell electron-pair repulsion) theory, such species should have a seesaw geometry, with the lone electron pair located in the equatorial position. However, such a simple molecular structure is known only for SF_4, an extremely reactive gas used as a mild fluorinating agent that can cleanly convert carbonyl and carboxyl groups into CF_2 and CF_3 moieties, respectively (Wang, 2004). This behaviour strongly contrasts with the exceptional stability of SF_6, a very heavy gas with extensive industrial applications. Conversely, SCl_4 is stable only below 243 K and is predicted to consist of a $Cl_3S^+Cl^-$ ion pair (Greenwood & Earnshaw, 1997). Such ion pairs have also been confirmed for $SeCl_4$, $SeBr_4$ and $TeCl_4$ (Born *et al.*, 1979, 1981*a*,*b*; Buss & Krebs, 1971). However, they associate into $(EX_4)_4$ tetramers forming E_4X_4 heterocubane cores, where each chalcogen atom is decorated by three terminal halogen atoms, and these terminal $E-X$ bonds are far shorter than the $E\cdots X$ interactions within the heterocubane core. Intriguingly, $SeCl_4$ and $SeBr_4$ form polymorphs due to different mutual orientations of these tetrameric $(SeX_4)_4$ units within the crystal (Born *et al.*, 1979, 1981*a*,*b*).

Furthermore, these $(EX_4)_4$ species are also prime examples of hypervalent compounds that do not adhere strictly to the Lewis octet rule and have thus garnered further attention. For example, in 1930, Simons published a synthesis of pure $SeCl_4$ and noted the central atom 'should be represented with a shell

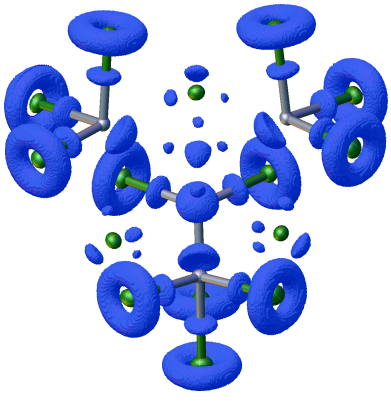

Table 1
Experimental details.

Crystal data	
Chemical formula	Se_4Cl_{16}
M_r	883.04
Crystal system, space group	Monoclinic, *C*2/*c*
Temperature (K)	100
a, *b*, *c* (Å)	16.31259 (16), 9.79402 (10), 14.76098 (14)
β (°)	116.9694 (4)
V (Å^3)	2101.83 (4)
Z	4
Radiation type	Mo $K\alpha$
μ (mm^{-1})	9.00
Crystal size (mm)	0.44 × 0.23 × 0.23
Data collection	
Diffractometer	Bruker SMART APEX DUO with an APEXII detector
Absorption correction	Multi-scan (*SADABS*; Krause *et al.*, 2015*a*)
T_{min}, T_{max}	0.037, 0.119
No. of measured, independent and observed [$I > 2\sigma(I)$] reflections	136263, 5097, 5007
R_{int}	0.036
(sin $\theta/\lambda)_{max}$ (Å^{-1})	0.833
Refinement	
$R[F^2 > 2\sigma(F^2)]$, $wR(F^2)$, S	0.012, 0.027, 1.28
No. of reflections	5097
No. of parameters	92
$\Delta\rho_{max}$, $\Delta\rho_{min}$ (e Å^{-3})	0.45, −0.39

Computer programs: *APEX2* (Bruker, 2007), *SAINT* (Bruker, 2007), *SHELXT2014* (Sheldrick, 2015*a*), *SHELXL2019* (Sheldrick, 2015*b*), *Mercury* (Macrae *et al.*, 2020) and *publCIF* (Westrip, 2010).

of ten electrons' (Simons, 1930). Furthermore, in 2002, Silvi used electron localization function (ELF) analysis on the gas phase form of the monomeric compounds AX_n (A = nonmetallic element of groups 13–17 and X = halogen) to prove that. in fact, the electronegativity of the ligands has a strong influence on the valence shell population of the central atom and that in these hypervalent compounds, the central atom usually has less than eight electrons in its valence shell (Noury *et al.*, 2002).

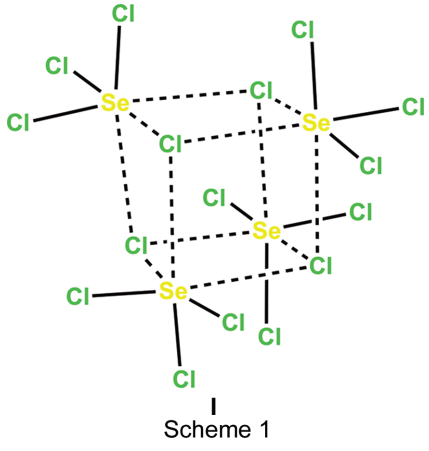

Scheme 1

In this sense, the concept of hypervalency attracted a lot of scrutiny and, recently, robust techniques for the determination of experimental charge densities and quantum crystallography were used to study the electronic nature of hypervalent compounds. Therefore, Stalke and co-workers used a multipolar refinement of K_2SO_4 to determine that, instead of double S═O bonds, the sulfate anion contains rather highly polarized single S—O bonds, discarding its hypervalent nature (Schmøkel *et al.*, 2012). Further studies by Grabowski and coworkers focused on extended wavefunction refinement of sulfate, phosphate and perchlorate species against high-resolution X-ray diffraction data, determining that, unlike sulfate and phosphate, that cannot be marked as hypervalent, hypervalency cannot be discarded for the perchlorate anion (Fugel *et al.*, 2019).

In this article, we report the electron-density analysis within the tetrameric solid-state structure of β-$(SeCl_4)_4$ (**1**) (Scheme 1) using Hirshfeld Atom Refinement (HAR) (Capelli *et al.*, 2014) based on single-crystal X-ray diffraction data.

2. Experimental

2.1. Sample preparation and mounting

Single crystals of the β-$SeCl_4$ phase were obtained directly from a commercial sample of $SeCl_4$ (Sigma–Aldrich/Merck) and were rinsed with thoroughly dried dichloromethane (Sigma–Aldrich/Merck) under an inert N_2 atmosphere. As $SeCl_4$ reacts immediately with nonhalogenated organic samples (including hydrocarbon oil), the crystals were placed in a Fomblin perfluoropolyether oil (Solvay) to avoid their decomposition, evidenced by the formation of red selenium on the surface. Attempts to mount the crystals on nylon loops failed due to the rapid disintegration of the nylon fiber in contact with $SeCl_4$. Therefore, the crystal was mounted on a spine from the Nopal Cactus (Opuntia littoralis), which proved to be inert and created less background during the measurement than a glass fibre.

2.2. Data collection and processing

The mounted crystal was placed in a stream of cold nitrogen gas at 100 K. The data were collected on a Bruker APEX DUO three-circle diffractometer equipped with an APEXII CCD detector and an Incoatec IμS microsource with Quazar mirrors using Mo $K\alpha$ radiation (λ = 0.71073 Å). 31 ω scans were collected at three different 2θ positions using 0.3° slicing, yielding a total of 18600 frames. During the data collection, a 90 μm thick aluminium filter was placed on the wider end of the collimator to remove the 5 keV radiation (Krause *et al.*, 2015*b*). The data were integrated with *SAINT* (Bruker, 2007). Corrections for absorption and oblique incidence, as well as scaling of the data, were performed using *SADABS* (Krause *et al.*, 2015*a*). This led to a data set with a maximum resolution of sin θ/λ = 0.833 Å^{-1} and average redundancy, I/σ, R_{sym} and R_σ of ∼26, 63.9, 0.0363 and 0.0105, respectively (see Table S1 in the supporting information). The structure was solved by direct methods (*SHELXT*; Sheldrick, 2015*a*) and refined using the independent atom model (IAM) with full-matrix least-squares on F^2 (*SHELXL* and *ShelXle*; Sheldrick, 2015*b*;

Hübschle *et al.*, 2011). Crystal data, data collection and structure refinement details are summarized in Table 1.

2.3. Hirshfeld Atom Refinement (HAR)

HAR (Capelli *et al.*, 2014) was performed with *OLEX2* (Dolomanov *et al.*, 2009), *ORCA* (Version 5.0.3; Neese *et al.*, 2020) and *NoSpherA2* (Kleemiss *et al.*, 2021) software, at the PBE/x2c-TZVPP (denoted HAR^{P}) and ωB97X /x2c-TZVPP (denoted HAR^{ω}) levels of theory (Perdew *et al.*, 1996; Chai & Head-Gordon, 2008; Pollak & Weigend, 2017). The positions and anisotropic displacement parameters of all atoms were refined. The obtained sets of Kohn–Sham orbitals were used to analyse the electron densities (*vide infra*).

2.4. QTAIM analysis

The sets of Kohn–Sham orbitals from the HAR were used to determine the local properties of the electron densities in the different HARs of **1** according to the Quantum Theory of Atoms in Molecules (Bader, 1990) using the *AIMAll* program package (Keith, 2019). The molecular graphs were plotted in *VMD* software from the atoms, bond critical points (BCPs), ring critical points (RCPs), cage critical points (CCPs) and bond path coordinates. The Espinosa–Mollins–Lecomte approximation was used to convert the potential energy at the BCP to interaction energy (Espinosa *et al.*, 1998).

2.5. Electron Localization Function (ELF)

The set of Kohn–Sham orbitals was used to generate the respective wavefunctions. The wavefunctions were used to determine the topological properties according to the ELF using the *Multiwfn* software (Lu & Chen, 2012). The ELF isosurface was plotted using *ChimeraX* software (Version 1.8; Meng *et al.*, 2023).

3. Results and discussion

3.1. Data collection and IAM refinement

As mentioned above, the synthesis of pure $SeCl_4$ was reported in 1930 by Simons, and two decades later, Gerding & Houtgraaf (1954) used the Raman spectra of $SeCl_4$ in the solid state to propose that it exists in the form of a $SeCl_3^+Cl^-$ ionic pair. In 1981, Kniep and co-workers published two articles describing the crystal structures of the thermodynamically stable α-$SeCl_4$ ($P\bar{4}3m$) and the metastable β-$SeCl_4$ ($C2/c$) phases, establishing their tetrameric $(SeCl_4)_4$ nature and a polymorphic relationship (Born *et al.*, 1981*a*,*b*). A low-temperature measurement (123 K) of the crystal structure of the β-$SeCl_4$ phase was reported by Richtera *et al.* (2014), but none of these data sets had the quality or resolution required for HAR. Therefore, we collected new data for the metastable β phase at 100 K. However, our first attempt revealed that, after approximately 1 d of measurement at 100 K, the crystal starts to decompose, as evidenced by increasing R_{sym} values for subsequent runs and the development of an intense reddish hue for the originally off-white crystal. A similar coloration was observed by Schürmann *et al.* (2022) during the measurement of Se_2Bn_2 (Bn = benzyl), where it was traced to the rupture of Se—Se and Se—C bonds due to radiation damage. Therefore, the collection strategy was adjusted to obtain a high-quality and redundancy data set with a resolution of $\sin\theta/\lambda = 0.833$ Å^{-1} in only a few hours. The β-$SeCl_4$ phase (**1**) crystallizes in the monoclinic space group $C2/c$ with half of the tetrameric species in the asymmetric unit, where the rest of the molecule is generated by a twofold axis ($-x+1$, y, $-z+\frac{1}{2}$). The crystal structure obtained from the Independent Atom Model (IAM) refinement can be seen in Fig. 1. Data collection and refinement details are given in Table 1.

The eight symmetry-independent Cl atoms around the two Se atoms can be divided into two groups: the first contains atoms Cl1–Cl6 which form terminal Se—Cl bonds and will be referred to as Cl_T, and Cl7 and Cl8 which are located at the corners of the Se_4Cl_4 heterocubane core (**1**) and will be referred to as Cl_C. This different bonding situation greatly affects the Se—Cl bond length, where the Se—Cl_T bonds are significantly shorter [2.1608 (2)–2.1962 (2) Å] than the Se—Cl_C bonds [2.7445 (2)–2.8358 (2) Å]. This suggests that the terminal Cl atoms are covalently bonded to Se, while the Se···Cl_C interactions are electrostatic. This Se—Cl bond-length difference also demonstrates the distortion of the $SeCl_6$ octahedron, which is further evident from the Cl_T—Se—Cl_T [94.900 (9)–96.953 (8)°], Cl_C—Se—Cl_C [88.605 (7)–89.657 (7)°] and Cl_T—Se—Cl_C [171.202 (7)–172.273 (7)°] bond angles. Table 2 contains the bond lengths and angles obtained from IAM, HAR^{P} and HAR^{ω} (*vide infra*). As can be seen, the geometry of **1** is identical within the s.u. values between the three models and as confirmed also by root-mean-square deviation (RMSD) values of 0.0001–0.0002.

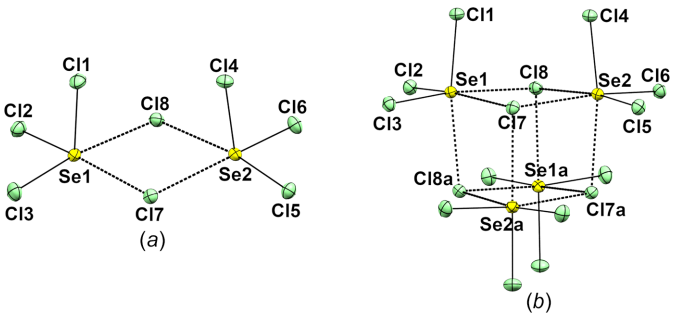

Figure 1
Crystal structure of β-$SeCl_4$ obtained from the IAM, showing (*a*) the asymmetric unit and (*b*) the tetramer conformation, with displacement ellipsoids at the 50% probability level.

3.2. Hirshfeld Atom Refinement (HAR)

As a next step, we focused on the HAR of the tetrameric molecule of β-$(SeCl_4)_4$ using the x2c-TZVPP basis set and different functionals. Based on the obtained integrated charges, we selected the PBE (HAR^{P}) and ωB97X (HAR^{ω}) functionals (Perdew *et al.*, 1996; Chai & Head-Gordon, 2008; Pollak & Weigend, 2017) for the final study as they led to the lowest and largest delocalization of the charge in the molecule.

Table 2
Selected bond lengths and angles of β-$(SeCl_4)_4$ from the independent atom model (IAM) and HAR.

Bond	IAM	HAR^P	HAR$^\omega$	Angle	IAM	HAR^P	HAR$^\omega$
Se1—Cl1	2.1649 (2)	2.1646 (2)	2.1646 (2)	Cl1—Se1—Cl2	96.452 (8)	96.455 (8)	96.456 (8)
Se1—Cl2	2.1835 (2)	2.1834 (2)	2.1833 (2)	Cl1—Se1—Cl3	96.559 (8)	96.564 (7)	96.566 (7)
Se1—Cl3	2.1608 (2)	2.1606 (2)	2.1605 (2)	Cl2—Se1—Cl3	96.731 (8)	96.733 (8)	96.733 (8)
Se1—Cl7	2.7534 (2)	2.7533 (2)	2.7534 (2)	Cl4—Se2—Cl5	95.440 (9)	95.443 (8)	95.443 (8)
Se1—Cl8*a*	2.8030 (2)	2.8030 (2)	2.8030 (2)	Cl4—Se2—Cl6	96.953 (8)	96.955 (8)	96.956 (8)
Se1—Cl8	2.8358 (2)	2.8358 (2)	2.8358 (2)	Cl5—Se2—Cl6	94.900 (9)	94.907 (8)	94.908 (8)
Se2—Cl4	2.1744 (2)	2.1742 (2)	2.1742 (2)	Cl1—Se1—Cl7	89.360 (7)	89.363 (6)	89.364 (6)
Se2—Cl5	2.1962 (2)	2.1960 (2)	2.1960 (2)	Cl1—Se1—Cl8	88.791 (7)	88.790 (6)	88.790 (6)
Se2—Cl6	2.1819 (2)	2.1817 (2)	2.1816 (2)	Cl4—Se2—Cl7	89.657 (7)	89.659 (7)	89.659 (7)
Se2—Cl7	2.7446 (2)	2.7445 (2)	2.7445 (2)	Cl4—Se2—Cl8	88.605 (7)	88.607 (7)	88.607 (7)
Se2—Cl8	2.7445 (2)	2.7445 (2)	2.7445 (2)	Cl1—Se1—Cl8*a*	172.273 (7)	172.266 (7)	172.265 (7)
Se2—Cl7*a*	2.7731 (2)	2.7730 (2)	2.7730 (2)	Cl4—Se2—Cl7*a*	171.202 (7)	171.194 (7)	171.194 (7)

Symmetry code: (*a*) $-x+1, y, -z+\frac{1}{2}$.

Table 3
Integrated atomic charges for the crystallographically independent atoms for HAR.

Atom	Se1	Se2	Cl1	Cl2	Cl3	Cl4	Cl5	Cl6	Cl7	Cl8
HAR^P	1.262	1.260	−0.259	−0.280	−0.251	−0.274	−0.292	−0.275	−0.438	−0.459
HAR$^\omega$	1.500	1.507	−0.288	−0.315	−0.269	−0.296	−0.326	−0.305	−0.591	−0.614

The set of Kohn–Sham orbitals based on the experimental geometry of the molecule was obtained with *ORCA* (Neese *et al.*, 2020) and was used to calculate the aspherical densities using *NoSpherA2* (Kleemiss *et al.*, 2021). The final refinement was carried out with *olex.refine* (Dolomanov *et al.*, 2009), and the cycle was repeated until convergence. The Meindl–Henn fractal dimension *versus* residual electron-density plot (Meindl & Henn, 2007) shows some unrefined residual electron density that can be ascribed mainly to an anharmonic motion of the Se atoms. However, its refinement would require a resolution of sin $\theta/\lambda = 1.35$ Å^{-1} (Kuhs, 1992) and was therefore not adopted (see Figs. S1 and S2 in the supporting information). Thus, the residual densities are about 0.44 e Å^{-3}, which is, however, only 1.3% of the electrons of an Se atom. Table S2 contains the final refinement parameters for the HAR. For each functional, we have made two refinements. The first considered only the tetrameric molecule and was used to calculate the molecular 2D and 3D maps, while the second included a cluster of 14 tetrameric molecules surrounding the central molecule that was used to evaluate the molecular properties and the intermolecular interactions (*vide infra*). In all cases, the resulting sets of Kohn–Sham orbitals were used for the following analyses.

3.3. QTAIM analysis

The Quantum Theory of Atoms in Molecules (QTAIM) analysis (Bader, 1990) of the local properties of the electron density obtained from the HAR^P and HAR$^\omega$ models of the tetrameric molecule of **1** revealed nearly identical molecular graphs (Fig. 2). However, there are significant differences in the integrated atomic charges (Table 3, and Tables S3 and S4) and the different descriptors of the electron density related to the BCPs (Table 4, and Tables S5 and S6). Both models lead to

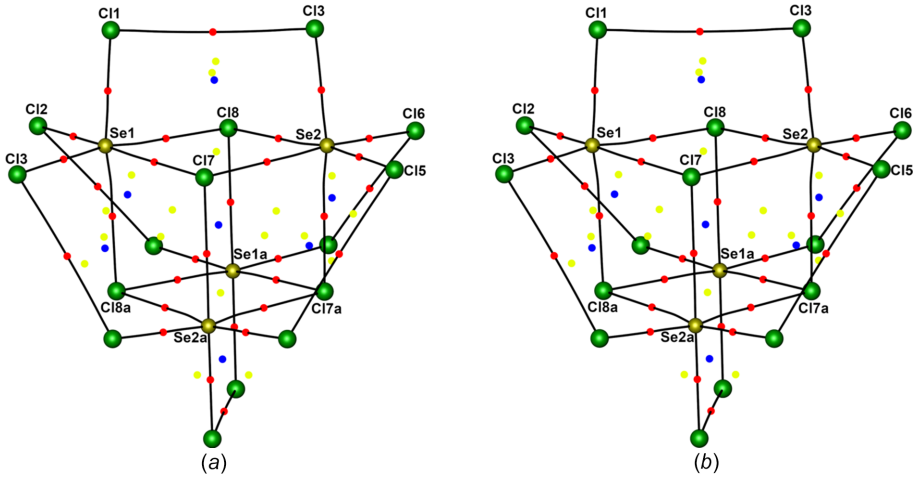

Figure 2
Molecular graph of (*a*) HAR^P and (*b*) HAR$^\omega$, and the distribution of bond critical points (BCPs, red), ring critical points (RCPs, yellow) and cage critical points (CCPs, blue).

Table 4
Topological properties, namely, density (ρ_{BCP}) and Laplacian ($\nabla^2\rho_{BCP}$), at the BCPs and bond lengths (Å) for selected Se—Cl bonds in **1**, obtained from HAR^P and HAR$^\omega$ (in parentheses).

Bond	ρ_{BCP} (e Å^{-3})	$\nabla^2\rho_{BCP}$ (e Å^{-5})	Bond length	ε
Se1—Cl1	0.851 (0.885)	−0.011 (−1.261)	2.165 (2.165)	0.01 (0.01)
Se1—Cl2	0.821 (0.853)	0.191 (−1.000)	2.184 (2.184)	0.01 (0.02)
Se1—Cl3	0.858 (0.893)	−0.082 (−1.363)	2.161 (2.161)	0.01 (0.01)
Se2—Cl4	0.836 (0.870)	0.083 (−1.154)	2.174 (2.174)	0.01 (0.01)
Se2—Cl5	0.803 (0.834)	0.274 (−0.890)	2.196 (2.197)	0.01 (0.02)
Se2—Cl6	0.824 (0.857)	0.175 (−1.032)	2.182 (2.182)	0.01 (0.01)
Se1—Cl7	0.267 (0.258)	1.808 (1.924)	2.755 (2.756)	0.01 (0.01)
Se1—Cl8	0.227 (0.219)	1.652 (1.772)	2.838 (2.839)	0.01 (0.01)
Se1—Cl8*a*	0.242 (0.233)	1.712 (1.833)	2.805 (2.806)	0.01 (0.02)
Se2—Cl7	0.272 (0.264)	1.810 (1.929)	2.746 (2.747)	0.01 (0.01)
Se2—Cl7*a*	0.257 (0.249)	1.771 (1.896)	2.774 (2.776)	0.01 (0.01)
Se2—Cl8	0.273 (0.264)	1.787 (1.899)	2.746 (2.747)	0.01 (0.01)

Symmetry code: (*a*) $-x+1, y, -z+\frac{1}{2}$.

very similar atomic charges ranging from −0.251 to −0.292 e for HAR^P and from −0.269 to −0.326 e for HAR$^\omega$ for the terminal Cl1–Cl6 atoms; however, the ωB97X functional gives ∼0.15 e higher atomic charges of the bridging Cl7 and Cl8 atoms (−0.591 and −0.614 e for HAR$^\omega$ *versus* −0.438 and −0.459 e for HAR^P). As a result, the hybrid functional ωB97X also leads to significantly higher selenium charges (1.500 and 1.507 e *versus* 1.262 and 1.260 e) and, therefore, to a significantly higher degree of electron localization in the $SeCl_3^+$ cation and the Cl^- anion. Although the Se—Cl_T bond lengths point to covalent bonds, these atomic charges and the respective average charge separation indexes (CSI) (Matta & Arabi, 2011) of 1.53 (HAR^P) and 1.80 e (HAR$^\omega$), respectively, reveal a significant ionic component of these bonds. Similarly, the distances and the higher charge of the Cl_C atoms point to purely electrostatic closed-shell Se···Cl_C interactions with even larger average CSIs of ∼1.71 and ∼2.14 e, respectively. Furthermore, as can be seen from Table 4, these different atomic charges are also accompanied by different values of the topological parameters, such as the density (ρ_{bcp}), Laplacian ($\nabla^2\rho_{bcp}$) and ellipticity (ε) at the BCPs. The virtually zero values for the ellipticity of all bonds and interactions are expected, owing to covalent–ionic Se—Cl_T single bonds and Se···Cl electrostatic interactions. Also, the significantly higher electron density at the BCPs of the Se—Cl_T bonds than that observed for the BCPs(Se···Cl_C) is compatible with such a bonding situation. Next, the $\nabla^2\rho_{bcp}$ provides additional useful information about the character of the interaction: when $\nabla^2\rho < 0$, there is an accumulation, and when $\nabla^2\rho > 0$, there is a depletion of charge density. In this sense, covalent bonds typically exhibit negative Laplacian values, while noncovalent interactions show positive values of the Laplacian. Thus, while

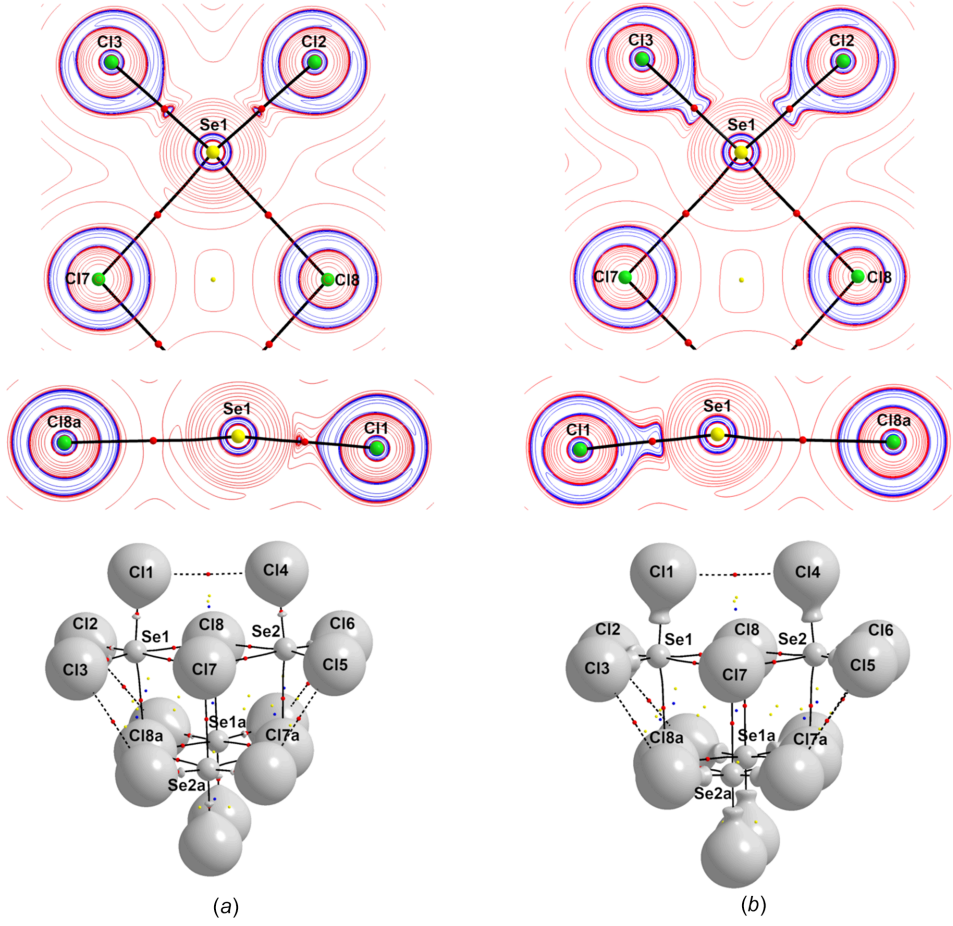

Figure 3
Laplacian density map in Cl_T—Se—Cl_T (top), the Cl_T—Se—Cl_C plane (middle) and the isosurface (bottom) of (*a*) HAR^P and (*b*) HAR$^\omega$ at zero isolevel ($\nabla^2\rho_{BCP}$ = 0 e A^{-5}).

the positive $\nabla^2\rho_{bcp}$ values for the Se···Cl_C interactions are similar for both methods and confirm closed-shell interactions between the nuclei, there are significant differences in the $\nabla^2\rho_{bcp}$ values for the Se—Cl_T bonds. While HAR$^{\omega}$ yields negative values (−0.890 to −1.363 e A^{-5}) congruent with a considerable covalent character of the bonds and, therefore, larger delocalization, HAR^{P} gives positive or only slightly negative values (−0.082 to 0.274 e A^{-5}), indicating the highly polarized nature of the Se—Cl_T bonds in this model. However, it is known that, especially for polar bonds, the Laplacian is very sensitive to even small variations in the position of the BCPs, as a change of only 0.02 Å can cause large changes in the Laplacian value or even in the sign due to very steep gradients along the bond path trajectory (Fig. S7). Such behaviour is also possible for the polar Se—Cl_T bond (electronegativity = 2.55 for Se and 3.16 for Cl). For a better visualization of these differences, Fig. 3 compares selected 2D and 3D maps of the Laplacian of **1** among the two methods. The maps clearly show the closed-shell nature of the Se···Cl_C interactions and the covalent nature of the Se—Cl_T bonds for the HAR$^{\omega}$ method. For HAR^{P}, one can observe the BCP between two regions of accumulation of electron density. However, no method shows the location of the stereoactive lone electron pair expected to be present on the Se atom.

3.4. Deformation density, Electron Localization Function (ELF) and Electrostatic Potential (ESP)

Deformation density analysis is one of the most important tools for determining regions where the valence electron density accumulates and is mainly associated with covalent bonds and lone pairs. Fig. 4 and Fig. S6 show the 3D deformation density isosurface maps of **1** obtained from *NoSpherA2* (Kleemiss *et al.*, 2021). The accumulation of the electron density in the Se—Cl_T bond regions confirms the covalent character of these bonds, while the Cl_C atoms have only noncovalent interactions with the Se atoms. Finally, each Se atom features an electron-density accumulation ascribable

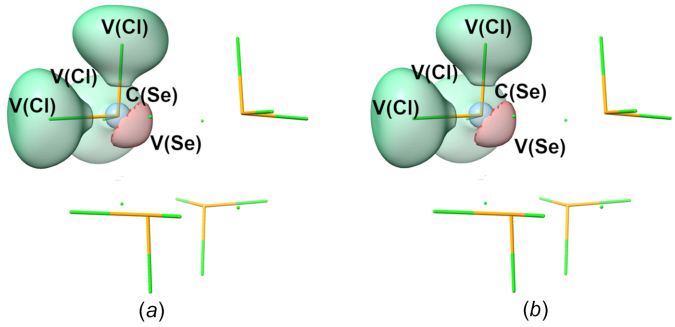

Figure 5
The localization domains of **1**. Core domains of Se atoms, C(Se), are represented in blue, unshared valence of Se atoms, V(Se), in red and valence shell of Cl atoms, V(Cl), in green for (*a*) HAR^{P} and (*b*) HAR$^{\omega}$.

to the stereoactive lone pair pointing to the centre of the Se_4Cl_4 heterocubane core. While these features are observed for both functionals, the map for the ω97X refinement points to more covalent Se—Cl_T bonds due to a larger localization of the electron density within the molecule in agreement with the previous analysis. Finally, the σ hole is clearly observable for all Cl_T atoms, while the valence density of the Cl_C atoms is rather localized into four lone-pair regions where three are oriented towards the Se atoms. Becke and Edgecombe's Electron Localization Function (ELF) (Becke & Edgecombe, 1990) is another tool that can be used to describe electronic localization. Similar to QTAIM, the topological analysis of ELF allows for the characterization of interatomic interactions present in a molecule through points known as critical points. A point at a local maximum is defined as an attractor, and the set of trajectories that end at this point define the attractor basin. There are two types of basins: core basins centred near the inner atomic shell and valence basins associated with intermolecular surfaces, where there are shared or lone pairs. Therefore, ELF was used to confirm the location of the lone electron pair of the Se atom in **1** (Fig. 5). Furthermore, the basin ascribed to V(Se) has an integrated population of 2.776 (2.432), V(Se,Cl) 0.898 (1.201) and V(Cl) 6.995 (6.740) elec-

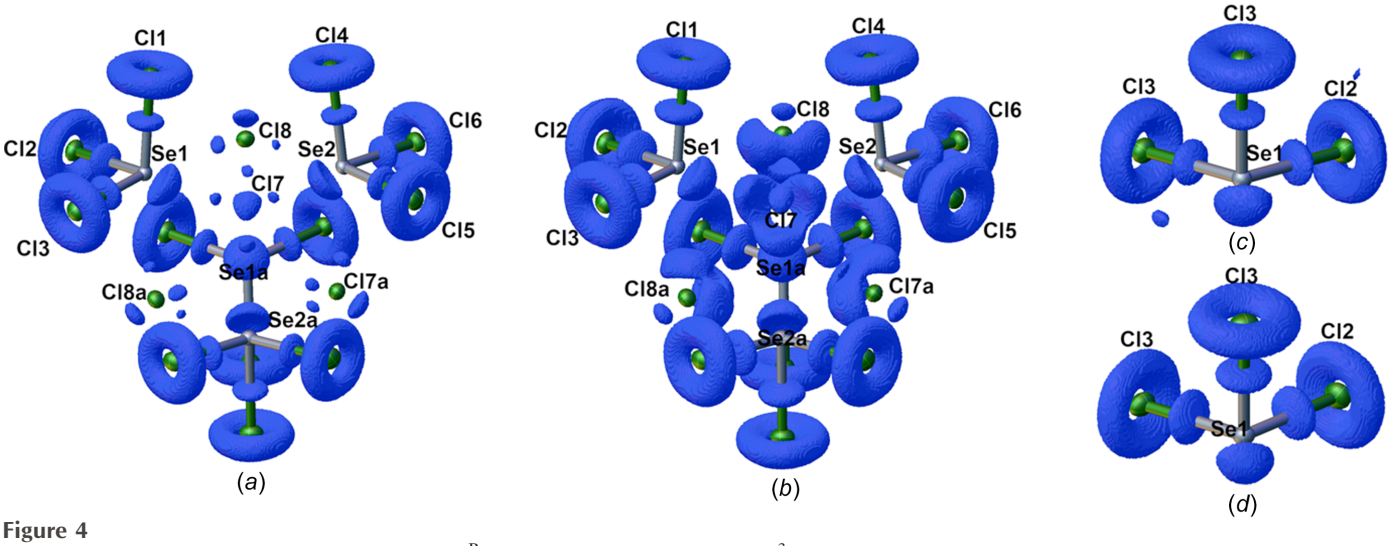

Figure 4
Deformation density isosurface from (*a*)/(*c*) HAR^{P} and (*b*)/(*d*) HAR$^{\omega}$ at 0.05 e A^{-3}.

Table 5
Selected EML interaction energies (kcal mol^{-1}) of Cl···Cl contacts obtained from HAR^{P} and HAR$^{\omega}$ (in parentheses).

Bond	G	V	E_{int}
Cl1···Cl4*a*	1.839 (1.892)	−1.245 (−1.311)	−0.623 (−0.656)
Cl1···Cl4*b*	3.140 (3.286)	−2.214 (−2.397)	−1.107 (−1.199)
Cl1···Cl6*c*	2.908 (3.013)	−2.011 (−2.136)	−1.005 (−1.068)
Cl1···Cl2*d*	2.649 (2.732)	−1.792 (−1.897)	−0.896 (−0.949)
Cl1···Cl1*d*	2.391 (2.454)	−1.590 (−1.674)	−0.795 (−0.837)
Cl1···Cl5*e*	1.511 (1.534)	−0.983 (−1.023)	−0.491 (−0.512)
Cl1···Cl4*f*	1.402 (1.427)	−0.929 (−0.970)	−0.464 (−0.485)
Cl1···Cl3*d*	1.105 (1.127)	−0.734 (−0.767)	−0.367 (−0.383)
Cl2···Cl2*a*	1.963 (2.023)	−1.342 (−1.417)	−0.671 (−0.708)
Cl2···Cl5*f*	2.649 (2.578)	−1.793 (−1.855)	−0.896 (−0.928)
Cl2···Cl2*d*	2.216 (2.533)	−1.520 (−1.762)	−0.760 (−0.881)
Cl2···Cl4*c*	2.128 (2.192)	−1.422 (−1.505)	−0.711 (−0.752)
Cl2···Cl8*c*	1.833 (1.893)	−1.173 (−1.305)	−0.586 (−0.652)
Cl2···Cl7*f*	1.604 (1.612)	−1.061 (−1.070)	−0.530 (−0.535)
Cl2···Cl4*f*	1.615 (1.557)	−1.037 (−1.047)	−0.519 (−0.524)
Cl2···Cl6*c*	1.469 (1.380)	−0.975 (−0.934)	−0.488 (−0.467)
Cl3···Cl1*a*	1.712 (1.757)	−1.155 (−1.213)	−0.578 (−0.606)
Cl3···Cl4*g*	2.460 (2.732)	−1.706 (−1.898)	−0.853 (−0.949)
Cl3···Cl7*f*	2.455 (2.292)	−1.667 (−1.616)	−0.834 (−0.808)
Cl3···Cl2*d*	2.128 (2.192)	−1.422 (−1.505)	−0.711 (−0.752)
Cl3···Cl6*h*	1.823 (1.848)	−1.207 (−1.212)	−0.604 (−0.606)
Cl3···Cl5*f*	1.592 (1.646)	−1.032 (−1.118)	−0.516 (−0.559)
Cl3···Cl5*h*	1.523 (1.632)	−1.000 (−1.077)	−0.500 (−0.538)
Cl3···Cl6*f*	1.351 (1.507)	−0.893 (−1.027)	−0.447 (−0.513)
Cl7···Cl1*f*	2.332 (2.435)	−1.578 (−1.713)	−0.789 (−0.856)
Cl7···Cl3*f*	1.824 (1.895)	−1.208 (−1.306)	−0.604 (−0.653)
Cl7···Cl7*f*	1.359 (1.420)	−0.915 (−0.996)	−0.458 (−0.498)

Symmetry codes: (*a*) $-x+1, y, -z+\frac{1}{2}$; (*b*) $-x+\frac{1}{2}, y-\frac{1}{2}, -z+\frac{1}{2}$; (*c*) $x+\frac{1}{2}, -y+\frac{1}{2}, z+\frac{1}{2}$; (*d*) $-x+1, -y, -z+1$; (*e*) $x, y-1, z$; (*f*) $-x+1, -y+1, -z+1$; (*g*) $-x+\frac{1}{2}, y-\frac{1}{2}, -z+\frac{1}{2}$; (*h*) $x, -y+1, z+\frac{1}{2}$.

trons in HAR^{P} (HAR$^{\omega}$). This confirms that the model obtained using the ωB97X functional describes the Se—Cl bonds as having greater covalent character compared to the PBE functional. The integration of the basins shows that there are more shared electrons in V(SeCl), which is consistent with the Laplacian and deformation density maps. It is noteworthy that the sum of the populations of V(SeCl) and V(Se) results in a total of 5.470 (6.035) electrons, in agreement with Silvi's proposition that the central atom has in its valence shell less than eight electrons and should therefore not be considered hypervalent.

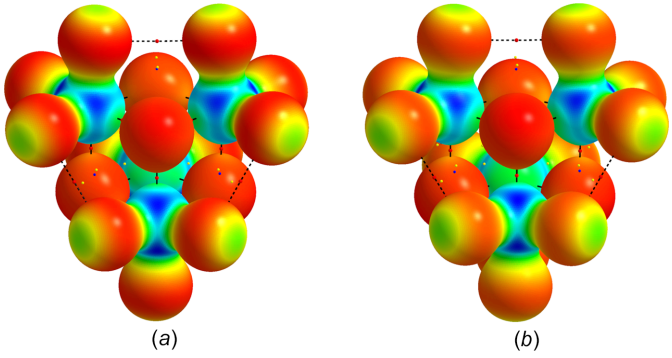

Figure 6
Isosurface of electron density with mapped electrostatic potential for (*a*) HAR^{P} and (*b*) HAR$^{\omega}$ at an $\rho(\mathbf{r})$ value of 0.05 e Å^{-3}. The minimum ESP values on the isosurface (0.141) are in red and the maximum ESP values on the isosurface (0.494) are in blue.

Table 6
Interaction energies (kcal mol^{-1}) calculated from the EML equation for all Se atom contacts.

Bond	G	V	E_{int}
Se1—Cl1	40.492 (37.419)	−81.054 (−81.054)	−40.527 (−41.523)
Se1—Cl2	38.939 (36.037)	−76.632 (−76.632)	−38.316 (−39.291)
Se1—Cl3	40.722 (37.553)	−81.981 (−81.981)	−40.991 (−41.989)
Se2—Cl4	39.629 (36.610)	−78.718 (−78.718)	−39.359 (−40.366)
Se2—Cl5	37.739 (34.912)	−73.693 (−73.693)	−36.847 (−37.808)
Se2—Cl6	39.090 (36.164)	−77.042 (−77.042)	−38.521 (−39.522)
Se1—Cl7	13.757 (14.340)	−15.745 (−15.745)	−7.873 (−8.078)
Se1—Cl8	11.713 (12.334)	−12.670 (−12.670)	−6.335 (−6.565)
Se1—Cl8*a*	12.470 (13.084)	−13.796 (−13.796)	−6.898 (−7.119)
Se2—Cl7	13.957 (14.586)	−16.130 (−16.130)	−8.065 (−8.306)
Se2—Cl7*a*	13.256 (13.914)	−14.982 (−14.982)	−7.491 (−7.742)
Se2—Cl8	13.813 (14.402)	−15.994 (−15.994)	−7.997 (−8.223)

Symmetry code: (*a*) $-x+1, y, -z+\frac{1}{2}$.

Finally, the Electrostatic Potential (ESP) was calculated for **1** and mapped onto the total electron density (Fig. 6). The mapped ESP shows regions of negative potential on the Cl atoms and positive potential on the Se atoms. The highest negative potential is on the Cl$_C$ atoms, corresponding to the strongest interactions. The Cl$_T$ atoms exhibit the highest potential in the equatorial region of the Cl atom and the lowest potential in the polar region in accordance with the σ-hole polarization observed in the deformation density maps. An interesting observation is that the ESP of the Se atom also shows a region of negative potential pointing towards the centre of the cage and is, therefore, related to the lone electron pair.

3.5. Crystal packing and intermolecular interactions

While the tetrameric molecule assembles mainly *via* cation–anion interactions, the crystal packing is dominated by weak Cl···Cl interactions (Table 5). To estimate the interaction energy of one molecule within the crystal, we have evaluated a cluster of 15 molecules, where the central molecule is surrounded by all close neighbours, mimicking the crystal packing. Herein, we use the Espinosa–Molins–Lecomte equation (EML) to evaluate the interaction energy (E_{int}) of the closed-shell interactions and to understand their influence on the crystal packing (Espinosa *et al.*, 1998). The interaction energy is determined from the local potential energy [$V(\mathbf{r})$] and the local kinetic energy [$G(\mathbf{r})$] at the position of the BCP according to the Abramov approach (Abramov, 1997). Table 6 shows the interaction energies calculated for all Se—Cl$_T$ and Se···Cl$_C$ bonds/interactions in **1**. Based on the results from HAR^{P}, the Se—Cl$_T$ bonds are, on average, about ∼39.1 kcal mol^{-1}, while the Se···Cl$_C$ interactions are, with an average energy of ∼7.4 kcal mol^{-1}, much weaker. The corresponding values derived from HAR$^{\omega}$ are ∼40.1 and ∼7.7 kcal mol^{-1}, respectively. In both cases, the Se—Cl$_T$ values are about half of the theoretical dissociation energy of 76.9 kcal mol^{-1} for the diatomic Se—Cl molecule (Luo, 2007). However, the high energy of the noncovalent Se···Cl$_C$ interactions suggests a significant influence on the stability of the tetrameric form of SeCl$_4$, as each Cl$_C$ atom forms three such

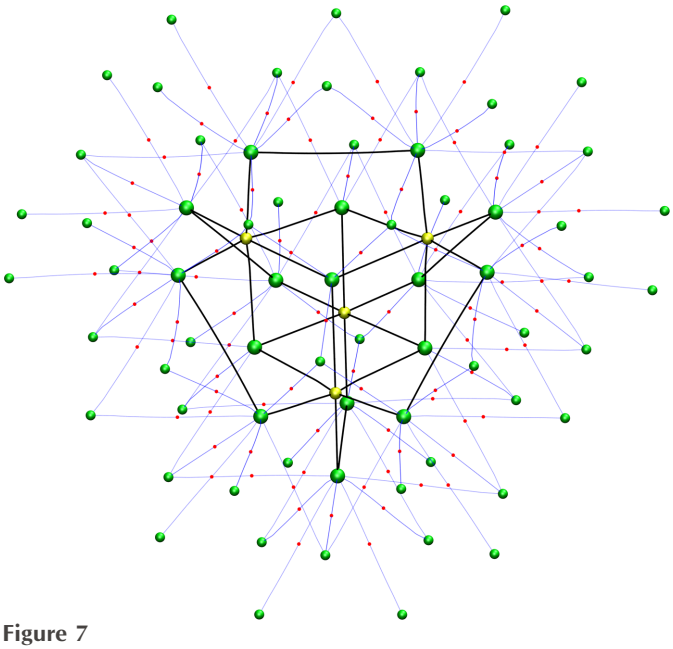

Figure 7
Molecular graph of the Cl···Cl contacts identified in the crystal packing of **1**.

interactions, bringing the total energy to more than half of the Se—Cl_T bond.

Additionally, the remaining interactions present in the crystal are all Cl···Cl contacts and can be divided into intra- and intermolecular. The intramolecular interactions form between two Cl_T atoms and are parallel to the Se···Se diagonal of each $Se_2(Cl_C)_2$ face of the heterocubane core (Fig. 7). There are, therefore, six such interactions per tetrameric molecule (each Cl_T forms only one) and they have average energies of −0.62 (for HAR^P) and −0.65 kcal mol^{-1} (for HAR^{ω}). Although their energies are rather small, the Cl···Cl contacts further stabilize the tetrameric arrangement as they directly link two Cl_3Se cationic units.

Next, each Cl_T atom forms seven additional intermolecular Cl···Cl interactions, while each Cl_C atom forms only three. In total, there are 96 intermolecular interactions originating from the tetrameric molecule, which explains the stability of the crystal packing. Table 5 shows selected interaction energies associated with one $Cl_3Se^+Cl^-$ unit, while Tables S7 and S8 contain additional details. Although all these intermolecular Cl···Cl interactions are weak [E_{int} = −0.219 (−0.227) to −1.108 (−1.200) kcal mol^{-1}], the sum of their energies is rather large: −60.0 and −63.6 kcal mol^{-1} for HAR^P and HAR^{ω}, respectively, revealing their significant contribution to the stabilization of the crystal packing. Overall, this analysis sheds more light on the stabilization of the tetrameric molecule and the crystal packing.

4. Conclusions

We present the analysis of the distribution of the electron density in the tetrameric molecule of β-$(SeCl_4)_4$ based on the models derived from Hirshfeld Atom Refinement (HAR). The molecule consists of four Cl_3Se^+ cations containing highly polarized Cl_T—Se closed-shell bonds and four Cl^- anions. These charged species assemble into a Se_4Cl_4 heterocubane core *via* closed-shell Cl_C···Se interactions that have only ∼19% of the energy of the Se—Cl_T bonds. However, each Cl^- anion forms three such interactions stabilizing the Se_4Cl_4 tetrameric core. The rather long Se···Cl_C distances (∼2.8 Å) are the result of the repulsion of the Cl^- anions with the stereoactive lone electron pairs of the Se atoms that point into the centre of the Se_4Cl_4 heterocubane core, as evidenced by ELF and deformation density maps. The tetrameric molecule is further stabilized by low-energy intramolecular Cl_T···Cl_T interactions linking two neighbouring Cl_3Se^+ cations. In the crystal, one tetrameric molecule forms numerous Cl···Cl contacts with energies lower than −1.2 kcal mol^{-1} per contact. However, the sum of all 96 of these contacts per tetramer rises to an interaction energy larger than 60 kcal mol^{-1}.

Acknowledgements

We are grateful to Professor Florian Kleemiss (RWTH Aachen University) for the continuous development of *NoSpherA2*. Molecular graphics of the ELF were created with UCSF *ChimeraX*, developed by the Resource for Biocomputing, Visualization, and Informatics at the University of California, San Francisco, with support from National Institutes of Health R01-GM129325 and the Office of Cyber Infrastructure and Computational Biology, National Institute of Allergy and Infectious Diseases.

Funding information

Funding for this research was provided by: Dirección General de Asuntos del Personal Académico from the UNAM (grant No. IN216224 to Vojtech Jancik); Dirección General de Cómputo y de Tecnologías de Información y Comunicación de la UNAM (grant No. LANCAD-UNAM-DGTIC-372 to Vojtech Jancik); Consejo Nacional de Humanidades, Ciencias y Tecnologías (grant No. 2328 to Vojtech Jancik; scholarship No. 855697 to Juan de Dios Guzmán Hernández).

References

Abramov, Yu. A. (1997). *Acta Cryst.* A**53**, 264–272.
Bader, R. F. W. (1990). In *Atoms in Molecules: A Quantum Theory*. Oxford University Press.
Becke, A. D. & Edgecombe, K. E. (1990). *J. Chem. Phys.* **92**, 5397–5403.
Born, P., Kniep, R. & Mootz, D. (1979). *Z. Anorg. Allg. Chem.* **451**, 12–24.
Born, P., Kniep, R. & Mootz, D. (1981*a*). *Z. Naturforsch. B*, **36**, 1516–1519.
Born, P., Kniep, R. & Mootz, D. (1981*b*). *Z. Naturforsch. B*, **36**, 1660–1662.
Bruker (2007). *SAINT* and *APEX*. Bruker AXS Inc., Madison, Wisconsin, USA.
Buss, B. & Krebs, B. (1971). *Inorg. Chem.* **10**, 2795–2800.
Capelli, S. C., Bürgi, H.-B., Dittrich, B., Grabowsky, S. & Jayatilaka, D. (2014). *IUCrJ*, **1**, 361–379.
Chai, D. & Head-Gordon, M. (2008). *J. Chem. Phys.* **128**, 084106.

Dolomanov, O. V., Bourhis, L. J., Gildea, R. J., Howard, J. A. K. & Puschmann, H. (2009). *J. Appl. Cryst.* **42**, 339–341.
Espinosa, E., Molins, E. & Lecomte, C. (1998). *Chem. Phys. Lett.* **285**, 170–173.
Fugel, M., Malaspina, L. A., Pal, R., Thomas, S. P., Shi, M. W., Spackman, M. A., Sugimoto, K. & Grabowsky, S. (2019). *Chem. Eur. J.* **25**, 6523–6532.
Gerding, H. & Houtgraaf, H. (1954). *Recl Trav. Chim. Pays Bas*, **73**, 737–747.
Greenwood, N. & Earnshaw, A. (1997). In *Chemistry of the Elements*, 2nd ed. London: Butterworth–Heinemann.
Hübschle, C. B., Sheldrick, G. M. & Dittrich, B. (2011). *J. Appl. Cryst.* **44**, 1281–1284.
Keith, T. A. (2019). *AIMAll*. TK Gristmill Software, Overland Park, KS, USA. https://aim.tkgristmill.com/.
Kleemiss, F., Dolomanov, O. V., Bodensteiner, M., Peyerimhoff, N., Midgley, L., Bourhis, L. J., Genoni, A., Malaspina, L. A., Jayatilaka, D., Spencer, J. L., White, F., Grundkötter-Stock, B., Steinhauer, S., Lentz, D., Puschmann, H. & Grabowsky, S. (2021). *Chem. Sci.* **12**, 1675–1692.
Krause, L., Herbst-Irmer, R., Sheldrick, G. M. & Stalke, D. (2015*a*). *J. Appl. Cryst.* **48**, 3–10.
Krause, L., Herbst-Irmer, R. & Stalke, D. (2015*b*). *J. Appl. Cryst.* **48**, 1907–1913.
Kuhs, W. F. (1992). *Acta Cryst.* A**48**, 80–98.
Lu, T. & Chen, F. (2012). *J. Comput. Chem.* **33**, 580–592.
Luo, Y.-R. (2007). *Comprehensive Handbook of Chemical Bond Energies*, 1st ed., pp. 9–67. Boca Raton: CRC Press.
Macrae, C. F., Sovago, I., Cottrell, S. J., Galek, P. T. A., McCabe, P., Pidcock, E., Platings, M., Shields, G. P., Stevens, J. S., Towler, M. & Wood, P. A. (2020). *J. Appl. Cryst.* **53**, 226–235.
Matta, C. F. & Arabi, A. A. (2011). *Future Med. Chem.* **3**, 969–994.
Meindl, K. & Henn, J. (2007). *Acta Cryst.* A**63**, s239.
Meng, E. C., Goddard, T. D., Pettersen, E. F., Couch, G. S., Pearson, Z. J., Morris, J. H. & Ferrin, T. E. (2023). *Protein Sci.* **32**, e4792.
Neese, F., Wennmohs, F., Becker, U. & Riplinger, C. (2020). *J. Chem. Phys.* **152**, 224108.
Noury, S., Silvi, B. & Gillespie, R. J. (2002). *Inorg. Chem.* **41**, 2164–2172.
Perdew, P., Burke, K. & Ernzerhof, M. (1996). *Phys. Rev. Lett.* **77**, 3865–3868.
Pollak, P. & Weigend, F. (2017). *J. Chem. Theory Comput.* **13**, 3696–3705.
Richtera, L., Jancik, V., Martínez-Otero, D., Pokluda, A., Zak, Z., Taraba, J. & Touzin, J. (2014). *Inorg. Chem.* **53**, 6569–6577.
Schmøkel, M. S., Cenedese, S., Overgaard, J., Jørgensen, M. R. V., Chen, Y.-S., Gatti, C., Stalke, D. & Iversen, B. B. (2012). *Inorg. Chem.* **51**, 8607–8616.
Schürmann, C. J., Teuteberg, T. L., Stückl, A. C., Ruth, P. N., Hecker, F., Herbst–Irmer, R., Mata, R. A. & Stalke, D. (2022). *Angew. Chem. Int. Ed.* **61**, e202203665.
Sheldrick, G. M. (2015*a*). *Acta Cryst.* A**71**, 3–8.
Sheldrick, G. M. (2015*b*). *Acta Cryst.* C**71**, 3–8.
Simons, J. H. (1930). *J. Am. Chem. Soc.* **52**, 3483–3487.
Wang, C.-L. J. (2004). *Sulfur Tetrafluoride*, in *Encyclopedia of Reagents for Organic Synthesis*, edited by L. Paquette. New York: John Wiley & Sons.
Westrip, S. P. (2010). *J. Appl. Cryst.* **43**, 920–925.

supporting information

Acta Cryst. (2024). C**80**, 766-774 [https://doi.org/10.1107/S2053229624010428]

Bonding properties and crystal packing in β-$(SeCl_4)_4$ derived from Hirshfeld Atom Refinement

Juan de Dios Guzmán-Hernández and Vojtech Jancik

Computing details

Tetra-μ_3-chlorido-dodecachloridotetraselenium

Crystal data

Se_4Cl_{16}
M_r = 883.04
Monoclinic, $C2/c$
a = 16.31259 (16) Å
b = 9.79402 (10) Å
c = 14.76098 (14) Å
β = 116.9694 (4)°
V = 2101.83 (4) Å^3
Z = 4
$F(000)$ = 1632
D_x = 2.791 Mg m^{-3}
Mo $K\alpha$ radiation, λ = 0.71073 Å
Cell parameters from 9693 reflections
θ = 2.5–50.5°
μ = 9.00 mm^{-1}
T = 100 K
Rhombic, colourless
0.44 × 0.23 × 0.23 mm

Data collection

Bruker SMART APEX DUO with an APEXII detector diffractometer
Radiation source: Incoatec IμS qith Quazar mirrors
Detector resolution: 8.333 pixels mm^{-1}
ω–scan
Absorption correction: multi-scan (SADABS; Krause *et al.*, 2015a)
T_{min} = 0.037, T_{max} = 0.119
136263 measured reflections
5097 independent reflections
5007 reflections with $I > 2\sigma(I)$
R_{int} = 0.036
θ_{max} = 36.3°, θ_{min} = 2.5°
h = −27→27
k = −16→16
l = −24→24

Refinement

Refinement on F^2
Least-squares matrix: full
$R[F^2 > 2\sigma(F^2)]$ = 0.012
$wR(F^2)$ = 0.027
S = 1.28
5097 reflections
92 parameters
0 restraints
Primary atom site location: structure-invariant direct methods
Secondary atom site location: difference Fourier map
$w = 1/[\sigma^2(F_o^2) + (0.0069P)^2 + 0.890P]$ where $P = (F_o^2 + 2F_c^2)/3$
$(\Delta/\sigma)_{max}$ = 0.006
$\Delta\rho_{max}$ = 0.45 e Å^{-3}
$\Delta\rho_{min}$ = −0.39 e Å^{-3}
Extinction correction: SHELXL2019 (Sheldrick, 2015b), $Fc^*=kFc[1+0.001xFc^2\lambda^3/\sin(2\theta)]^{-1/4}$
Extinction coefficient: 0.00034 (3)

Special details

Geometry. All esds (except the esd in the dihedral angle between two l.s. planes) are estimated using the full covariance matrix. The cell esds are taken into account individually in the estimation of esds in distances, angles and torsion angles; correlations between esds in cell parameters are only used when they are defined by crystal symmetry. An approximate (isotropic) treatment of cell esds is used for estimating esds involving l.s. planes.

Fractional atomic coordinates and isotropic or equivalent isotropic displacement parameters (Å²)

	x	*y*	*z*	U_{iso}*/U_{eq}
Se1	0.50248 (2)	0.23181 (2)	0.39049 (2)	0.01189 (2)
Se2	0.35906 (2)	0.52550 (2)	0.18171 (2)	0.01273 (2)
Cl1	0.39333 (2)	0.24449 (2)	0.43518 (2)	0.01637 (3)
Cl2	0.50124 (2)	0.00979 (2)	0.37648 (2)	0.01793 (3)
Cl3	0.61536 (2)	0.24339 (2)	0.54198 (2)	0.01706 (3)
Cl4	0.26097 (2)	0.51208 (2)	0.24339 (2)	0.01957 (3)
Cl5	0.37068 (2)	0.74902 (2)	0.19068 (2)	0.02076 (4)
Cl6	0.25887 (2)	0.52140 (2)	0.02147 (2)	0.01926 (3)
Cl7	0.50082 (2)	0.51209 (2)	0.37522 (2)	0.01420 (3)
Cl8	0.36760 (2)	0.24557 (2)	0.18441 (2)	0.01497 (3)

Atomic displacement parameters (Å²)

	U^{11}	U^{22}	U^{33}	U^{12}	U^{13}	U^{23}
Se1	0.01255 (3)	0.01113 (3)	0.01213 (3)	−0.00004 (2)	0.00572 (2)	0.00026 (2)
Se2	0.01165 (3)	0.01276 (3)	0.01371 (3)	0.00156 (2)	0.00568 (2)	0.00132 (2)
Cl1	0.01548 (7)	0.01822 (7)	0.01771 (7)	−0.00189 (5)	0.00954 (6)	−0.00117 (5)
Cl2	0.02442 (8)	0.01151 (6)	0.01908 (7)	−0.00001 (6)	0.01093 (6)	0.00042 (5)
Cl3	0.01562 (7)	0.01937 (8)	0.01345 (7)	0.00144 (6)	0.00418 (5)	0.00025 (5)
Cl4	0.01579 (7)	0.02482 (9)	0.02106 (8)	0.00400 (6)	0.01095 (6)	0.00340 (6)
Cl5	0.02390 (9)	0.01308 (7)	0.02485 (9)	0.00273 (6)	0.01065 (7)	0.00159 (6)
Cl6	0.01474 (7)	0.02493 (9)	0.01506 (7)	0.00155 (6)	0.00409 (6)	0.00235 (6)
Cl7	0.01451 (6)	0.01370 (6)	0.01458 (6)	0.00011 (5)	0.00676 (5)	−0.00124 (5)
Cl8	0.01407 (6)	0.01562 (7)	0.01511 (7)	−0.00181 (5)	0.00652 (5)	−0.00033 (5)

Geometric parameters (Å, º)

Se1—Cl3	2.1608 (2)	Se2—Cl4	2.1744 (2)
Se1—Cl1	2.1649 (2)	Se2—Cl6	2.1819 (2)
Se1—Cl2	2.1835 (2)	Se2—Cl5	2.1962 (2)
Se1—Cl7	2.7534 (2)	Se2—Cl8	2.7445 (2)
Se1—Cl8^{i}	2.8030 (2)	Se2—Cl7	2.7446 (2)
Se1—Cl8	2.8358 (2)	Se2—Cl7^{i}	2.7731 (2)
Cl3—Se1—Cl1	96.559 (8)	Cl4—Se2—Cl5	95.440 (9)
Cl3—Se1—Cl2	96.731 (8)	Cl6—Se2—Cl5	94.900 (9)
Cl1—Se1—Cl2	96.452 (8)	Cl4—Se2—Cl8	88.605 (7)
Cl3—Se1—Cl7	90.258 (7)	Cl6—Se2—Cl8	90.316 (7)
Cl1—Se1—Cl7	89.360 (7)	Cl5—Se2—Cl8	172.959 (8)

Cl2—Se1—Cl7	170.322 (7)	Cl4—Se2—Cl7	89.657 (7)
Cl3—Se1—Cl8^{i}	87.926 (7)	Cl6—Se2—Cl7	172.167 (8)
Cl1—Se1—Cl8^{i}	172.273 (7)	Cl5—Se2—Cl7	88.626 (7)
Cl2—Se1—Cl8^{i}	89.240 (7)	Cl8—Se2—Cl7	85.631 (6)
Cl7—Se1—Cl8^{i}	84.316 (6)	Cl4—Se2—Cl7^{i}	171.202 (7)
Cl3—Se1—Cl8	171.921 (7)	Cl6—Se2—Cl7^{i}	89.185 (7)
Cl1—Se1—Cl8	88.791 (7)	Cl5—Se2—Cl7^{i}	90.287 (7)
Cl2—Se1—Cl8	88.646 (7)	Cl8—Se2—Cl7^{i}	85.051 (6)
Cl7—Se1—Cl8	83.731 (6)	Cl7—Se2—Cl7^{i}	83.796 (6)
Cl8^{i}—Se1—Cl8	86.115 (6)	Se2—Cl7—Se1	96.042 (6)
Cl4—Se2—Cl6	96.953 (8)	Se2—Cl8—Se1	94.165 (6)

Symmetry code: (i) −*x*+1, *y*, −*z*+1/2.